

# Graph Neural Networks as Fast and High-fidelity Emulators for Finite-Element Ice Sheet Modeling

Maryam Rahnemoonfar<sup>1,2,\*</sup> and Younghyun Koo<sup>1</sup>

<sup>1</sup>Department of Computer Science and Engineering, Lehigh University, Bethlehem, PA, USA

<sup>2</sup>Department of Civil and Environmental Engineering, Lehigh University, Bethlehem, PA, USA

\*e-mail: maryam@lehigh.edu

## ABSTRACT

Although the finite element approach of the Ice-sheet and Sea-level System Model (ISSM) solves ice dynamics problems governed by Stokes equations quickly and accurately, such numerical modeling requires intensive computation on central processing units (CPU). In this study, we develop graph neural networks (GNN) as fast surrogate models to preserve the finite element structure of ISSM. Using the 20-year transient simulations in the Pine Island Glacier (PIG), we train and test three GNNs: graph convolutional network (GCN), graph attention network (GAT), and equivariant graph convolutional network (EGCN). These GNNs reproduce ice thickness and velocity with better accuracy than the classic convolutional neural network (CNN) and multi-layer perception (MLP). In particular, GNNs successfully capture the ice mass loss and acceleration induced by higher basal melting rates in the PIG. When our GNN emulators are implemented on graphic processing units (GPUs), they show up to 50 times faster computational time than the CPU-based ISSM simulation.

## Introduction

The recent warming climate has caused Greenland and the Antarctic ice sheets to lose more than 7500 Gt of ice from 1992 to 2020, contributing to approximately 21 mm of global sea level rise<sup>1</sup>. In Antarctica, the Pine Island Glacier (PIG) has experienced the most rapid mass loss and speedups, which were primarily driven by melt-driven thinning near the grounding line and calving events<sup>2-4</sup>. Consequently, the fast movement and melting of the PIG has contributed to more than 20 % of the total sea level rise of Antarctica<sup>5</sup>. In the context of fast-melting ice sheets and their impacts on the sea level rise, it is important to model the behavior of the Antarctic ice sheets accurately. For the last few decades, scientists have proposed several models to explain the thermomechanical flows of ice sheets. In those modeling studies, ice is commonly regarded as viscous non-Newton fluid that follows the Stokes equation<sup>6</sup>.

On the basis of Stokes equation, the dynamic mechanisms of large ice sheets are described by several simplified approximations, e.g., Shallow Ice Approximation (SIA)<sup>7</sup>, Shallow Shelf Approximation (SSA)<sup>8</sup>, Blatter-Pattyn approximation (BP)<sup>9,10</sup>, or a full-Stokes model (FS)<sup>11</sup>. The ISSM (Ice-sheet and Sea-level System Model) thermomechanical numerical model provides solutions for these four different ice flow models leveraging a finite element approach<sup>12</sup>. The unique characteristics of the ISSM model can be summarized as follows: (1) finite element methods, (2) fine mesh adaptation, and (3) parallel technologies. First, by using instructed meshes, the ISSM provides efficient ice flow solutions of high resolutions in areas where ice flow dynamics is critical. Second, the anisotropic mesh refinement allows ISSM to allocate its computational resources to the fine-resolution area of fast ice and coarse-resolution areas of stagnant ice. Finally, state-of-the-art parallel technologies make it possible to reduce the computation time via massive computer clusters.

Despite such advantages of ISSM in reducing computational time via adopting parallel technologies, implementing the ISSM model is only available through multi-core central processing units (CPU) because every finite element has to be solved one at a time in ice flow modeling. However, recently, graphic processing units (GPU) have emerged as an attractive alternative processor to CPUs because of their merit in parallel processing. GPUs divide a given task into a number of small tasks and process them parallelly, which allows a magnificent speed-up compared to serial processing by CPU. Therefore, although the parallel computation of GPUs cannot directly solve the governing equations of ice flow, machine learning based on GPUs can be potentially used as statistical emulators to accelerate the computational time on ice sheet modeling.

Deep learning techniques have been actively applied as statistical emulators for ice sheet modeling<sup>13-16</sup>. Convolutional neural networks (CNN) of the Instructed Glacier Model (IGM)<sup>13</sup> mimicked the ice flow simulations retrieved from the PISM (Parallel Ice Sheet Model) and CfsFlow models which are equipped with hybrid SIA + SSA and Stokes equations at different spatial resolutions. This IGM framework was also combined with a physics-informed neural network (PINN) to reduce the dependence on an instructor model by introducing an optimization function minimizing the energy associated with ice-flow

equations<sup>14</sup>. A similar CNN emulator was also used to retrieve ice flow for the inversion of ice thickness and basal conditions<sup>15</sup>. Beyond CNN, a neural operator called DeepONet<sup>17</sup> was used as a hybrid ice sheet dynamics surrogate model by adopting a finite element discretization for ice momentum equations<sup>16</sup>. However, to our knowledge, there have been no attempts to speed up the ISSM models using deep learning emulators and GPUs.

In this study, we aim to develop deep-learning emulators (a.k.a. surrogate models) of the ISSM model, selecting the PIG as the test site. To take full advantage of the finite element and mesh adaption of the ISSM, we specifically employ graph neural networks (GNNs) instead of the traditional CNN that have been mainly used in previous studies<sup>13–15</sup>. Even though traditional CNNs have the strength to recognize spatial patterns of Euclidean or grid-like structures (e.g., images) by using fixed-size trainable localized filters, they cannot be used for non-Euclidean or irregular structures where the connections to neighbors are not fixed<sup>18</sup>. Instead, GNNs have been more broadly utilized for irregular structures, including molecular structures, point clouds, social networks, and natural language processing<sup>18</sup>. Given that the meshes of ISSM have irregular graph-like structures tuned by ice flow, GNNs are more appropriate than other deep-learning architectures for the ISSM ice sheet modeling. In this study, we substitute the meshes of ISSM with graph structures and design several GNNs that imitate the ability of the ISSM to model ice thickness and flow. We evaluate the potential of various GNN architectures as ISSM emulators by comparing their fidelity and computational efficiency with CPU-based ISSM simulations and other traditional non-graph neural networks.

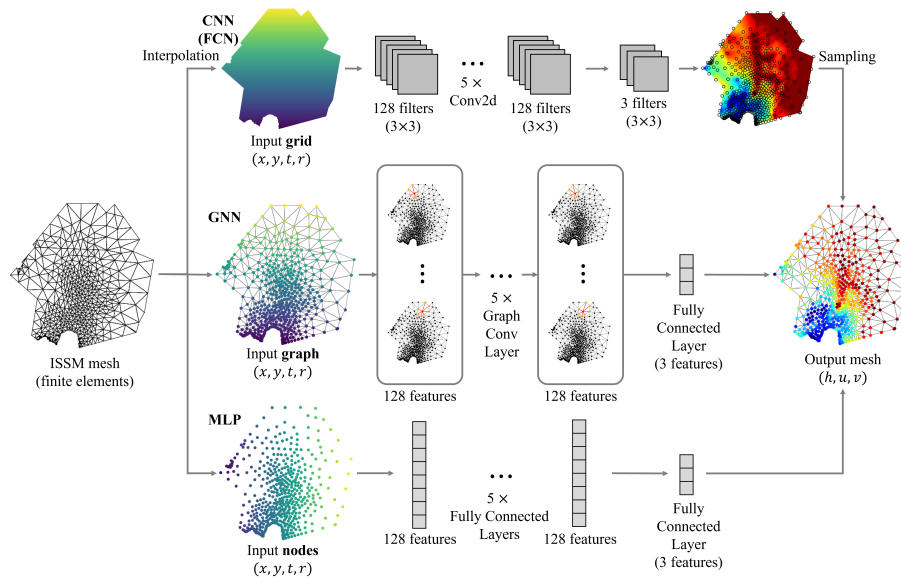


**Figure 1.** Schematic illustration of the deep-learning emulators used in this study (fully convolutional network, graph neural network, and multi-layer perceptron). In the case of the GAT and EGCN, the graph convolutional layers are replaced by graph attention layers and equivariant graph convolutional layers, respectively.

## Results

As the deep learning emulators for the ISSM simulation, we experiment with three GNNs: graph convolutional network (GCN), graph attention network (GAT), and equivariant graph convolutional network (EGCN). The graph structures of GNNs are generated by using the finite element meshes of the ISSM simulation as nodes and edges (Fig. 1). The graph nodes are iteratively updated through a series of graph convolutional layers by exchanging messages between the neighboring nodes connected by edges. Besides the three GNNs, one multi-layer perceptron (MLP) network and one convolutional neural network (CNN), particularly a fully convolutional network (FCN), are also assessed as traditional reference deep learning emulators. The MLP model uses the individual nodes of graph structures as input, but the connecting edges between nodes are not embedded in the MLP architecture. The CNN architecture can intrinsically embrace the neighboring information between nodes in regular grids through weights of the convolutional kernels, but the kernel size is fixed for all locations. In summary, the MLP does not use any spatial neighboring information between nodes; the CNN uses only the fixed neighboring information for all nodes; GNN uses different neighboring information between nodes determined by their node-edge connectivity. The details about these deep learning models are described in the Methods section. We evaluate the fidelity and computational efficiency of these deep learning emulators by training and testing them with ISSM transient simulation datasets for the PIG region: ice thickness and ice velocity modeled by SSA for 20 years with three different initial mesh sizes ( $M_0$ ) of 5 km, 10 km, and 20 km.

## Ice thickness

Table 1 shows the overall accuracy of ice thickness represented by root mean square error (RMSE) and correlation coefficient (R) for three mesh sizes. All deep learning emulators exhibit good agreements with the ISSM simulations with R greater than 0.997. When comparing the accuracy for different mesh sizes, the RMSEs of GNNs decrease, and correlation coefficients increase with larger mesh sizes. However, the mesh size does not significantly impact the accuracy of FCN and MLP. It should be noted that the EGCN model has better accuracy than the others for all mesh sizes, reducing RMSE by 5-10 m compared to the second-best model. In particular, for the 5 km initial mesh experiment, the EGCN is the only GNN emulator that outperforms the MLP and CNN (Table 1). This implies that the equivariance to rotations, translations, and permutations preserved by the EGCN can guarantee a better generality of the emulator regardless of mesh sizes, while other GNNs show low fidelity in a finer mesh structure.

**Table 1.** Accuracy of ice thickness for four deep learning emulators with different mesh resolutions. All metrics are averaged for the 0, 20, 40, and 60 m/year melting rates. The best accuracy for each mesh size is highlighted in bold.

Model	$M_0 = 5$ km		$M_0 = 10$ km		$M_0 = 20$ km	
	RMSE (m)	R	RMSE (m)	R	RMSE (m)	R
FCN	45.39	0.997	52.59	0.997	48.13	0.997
MLP	48.31	0.997	40.22	0.998	42.24	0.998
GCN	49.05	0.997	42.95	0.998	28.43	0.999
GAT	55.57	0.996	31.82	0.999	26.38	0.999
EGCN	<b>37.77</b>	<b>0.998</b>	<b>26.27</b>	<b>0.999</b>	<b>16.63</b>	<b>1.000</b>

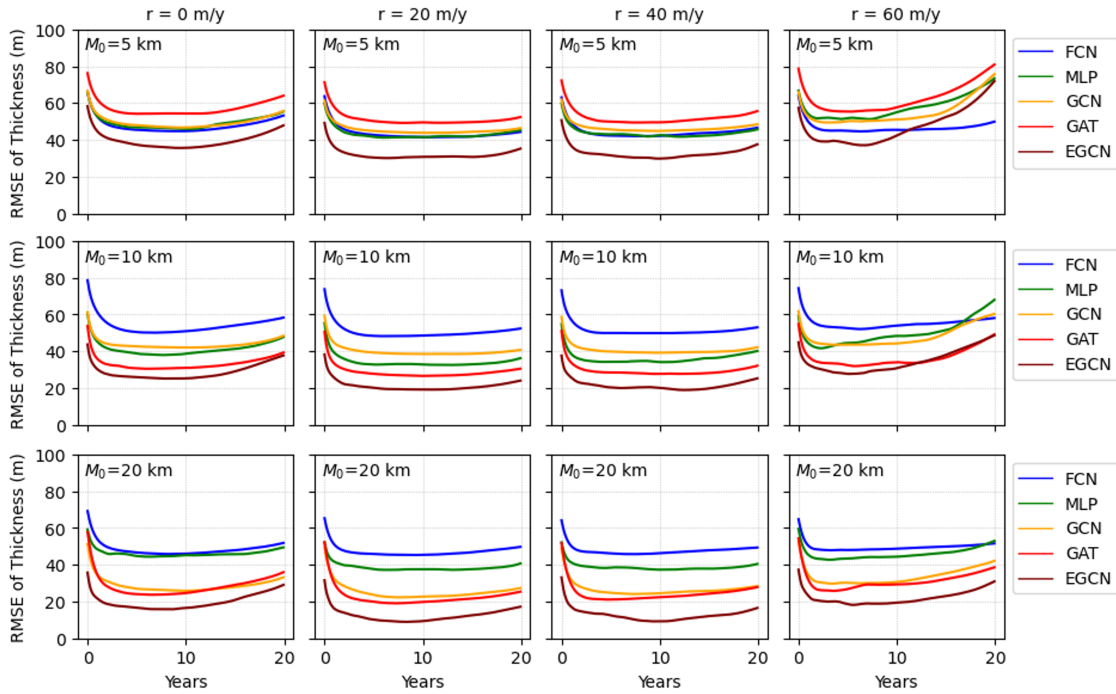


**Figure 2.** RMSE of ice thickness by years for different basal melting rates ( $r$ ) and initial mesh sizes ( $M_0$ ).

Fig. 2 shows the RMSE of ice thickness by years for four different basal melting rates (i.e., 0, 20, 40, and 60 m/year) and three different initial mesh sizes (i.e., 5 km, 10 km, and 20 km). The EGCN shows the lowest RMSE over 20-year transient simulation for all melting rates and mesh sizes. In all cases, the RMSE decreases from the initial condition to around year 10 and then increases slightly until year 20. The RMSE of ice thickness for a 60 m/year melting rate experiment rises more rapidly compared to the other melting rates. Dramatic changes in ice flow under a higher melting rate scenario can make it difficult for deep learning emulators to replicate such a rapid change (see the discussion section for more details).

The maps of ice thickness from the ISSM simulation and deep learning emulators are depicted in Fig. 3. The overall spatial distribution of ice thickness is well produced by deep-learning emulators: thicker ice ( $> 2000$  m) on the northeast side and

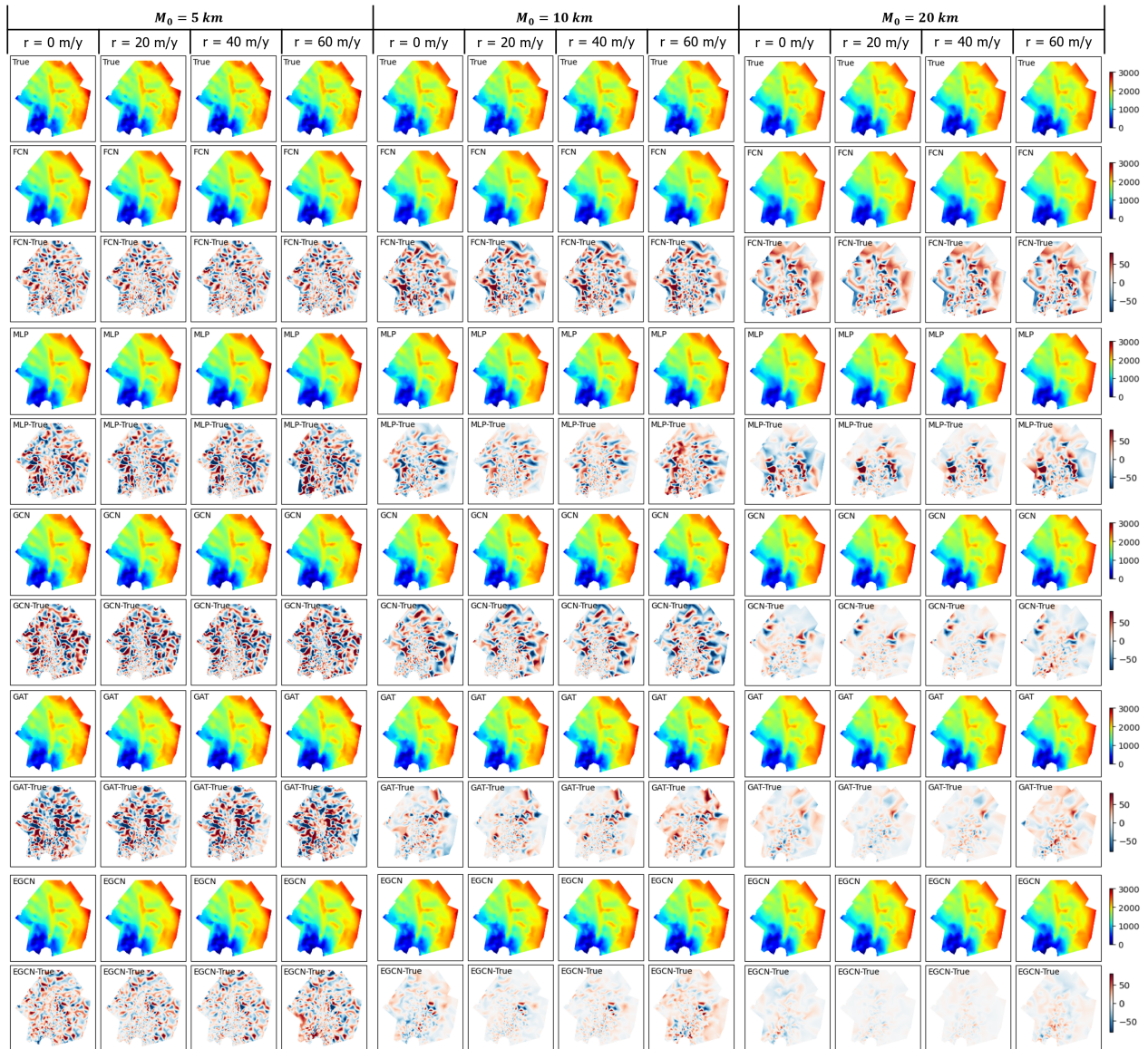


**Figure 3.** Maps of ice thickness modeled by the ISSM simulation (indicated as True) and difference with deep-learning emulators (FCN, MLP, GCN, GAT, and EGCN) for different basal melting rates ( $r$ ) and initial mesh sizes ( $M_0$ ). All maps are bilinearly interpolated from the node predictions and represent the average of 20-year results.

thinner ice on the south side near the coast ( $< 1000$  m). In Fig. 3, it is evident that the EGNN yields much less uncertainty than the other models over the entire PIG region. Moreover, while the other models show relatively large uncertainties in marginal areas with slow ice flow, the uncertainties by the EGCN are somehow evenly distributed around the PIG region.

### Ice velocity

RMSE and R of ice velocity are shown in Table 2. Although all deep learning models show good agreements with the ISSM simulation results with  $R > 0.997$ , EGCN shows the best accuracy among them. EGCN outperforms other emulators, particularly in a fine mesh size (5 km), reducing RMSE by 13.62 m/year compared to GCN. Even though GAT shows better accuracy than EGCN in 10 km mesh size, their RMSE difference is only 1.21 m/year. Similar to the ice thickness results, the RMSE of ice velocity also decreases with larger mesh sizes (fewer nodes) for graph neural networks. The RMSEs of ice velocity from FCN and MLP also decrease with larger mesh sizes.

Fig. 4 shows the RMSE of ice velocity by years for different melting rates. In general, the EGCN shows the lowest RMSE over 20-year transient simulation for most of the melting rates and mesh sizes. However, for some melting rates, mesh size, and years, GAT outperforms EGCN (e.g.,  $r=40$  m/year and  $r=60$  m/year with  $M_0=10$  km). Similar to the ice thickness, the RMSE is

**Table 2.** Accuracy of ice velocity for four deep learning emulators with different mesh resolutions. All metrics are averaged for the 0, 20, 40, and 60 m/year melting rates. The best accuracy for each mesh size is highlighted in bold.

Model	$M_0 = 5$ km		$M_0 = 10$ km		$M_0 = 20$ km	
	RMSE (m/year)	R	RMSE (m/year)	R	RMSE (m/year)	R
FCN	111.78	0.996	97.86	0.996	89.01	0.995
MLP	78.86	0.997	57.41	0.998	42.54	0.999
GCN	71.70	0.998	55.31	0.999	36.70	0.999
GAT	81.88	0.998	<b>41.87</b>	<b>0.999</b>	35.07	0.999
EGCN	<b>58.08</b>	<b>0.999</b>	43.08	0.999	<b>30.04</b>	<b>0.999</b>

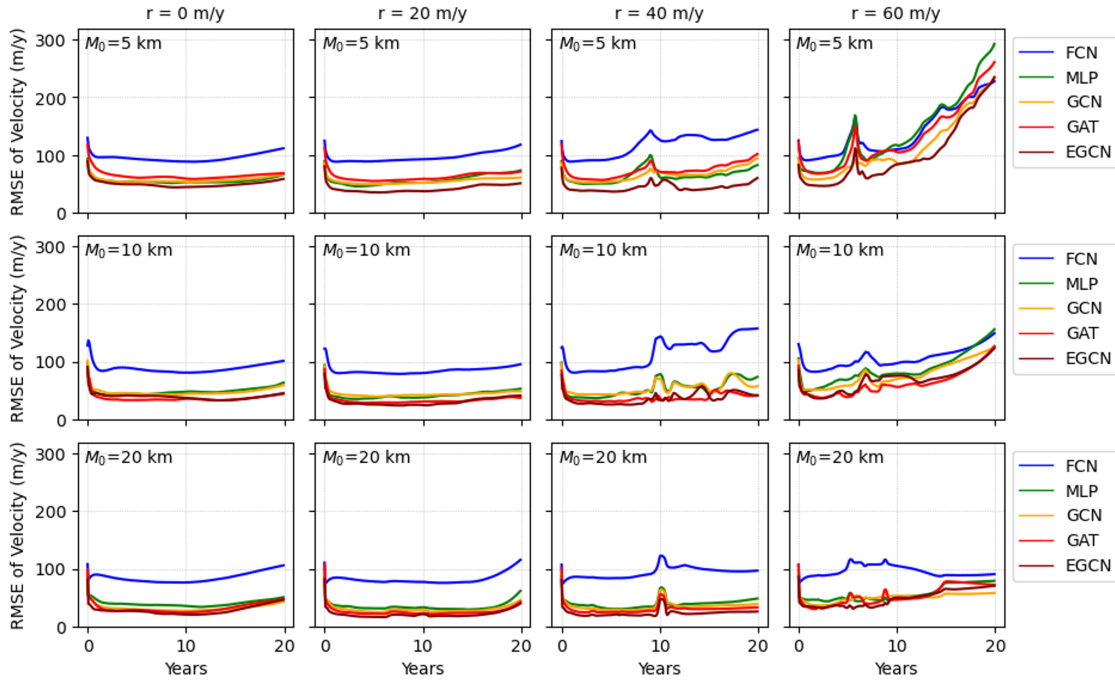


**Figure 4.** RMSE of ice velocity by years for different basal melting rates ( $r$ ) and initial mesh sizes ( $M_0$ ).

relatively high at the initial condition. At lower melting rates, RMSE remains consistent afterward. However, at higher melting rates, the RMSE rises as the year passes. Consequently, the RMSE reaches higher than 200 m/year in the last year at 60 m/year melting rate. This might be caused by the faster ice flow under higher melting rates; since ice flows faster as time passes under a higher melting rate, it is somehow difficult for the deep learning emulators to learn such dramatic variations in ice flow.

The spatial distribution of ice thickness from the ISSM simulation and deep learning emulators are shown in Fig. 5. The overall spatial distribution of ice velocity is well reproduced by deep-learning emulators: slow ice flow around ice margins and higher velocity under higher melting rates. Interestingly, most large errors are found along the main ice stream and branches of this ice stream in the FCN, MLP, GCN, and GAT test results. In particular, the error of FCN is mostly concentrated around the fast ice regions. This result implies that the fixed kernel size of FCN cannot efficiently reproduce different neighboring impacts by different ice velocity fields. Since most of the target area is covered by slow ice, the fixed kernel of FCN has limitations in representing a minor portion of fast ice. Hence, considering that EGCN significantly reduces the errors in the fast ice stream in Fig. 5, EGCN is more reliable for predicting fast ice behavior in the PIG than the traditional FCN.

### Computational performance

The main contribution of the deep learning emulators is to reduce the computational time by exclusively using GPUs. The total elapsed times for generating the transient results from the ISSM and deep learning models are in Table 3. GNN and MLP emulators take less time than the ISSM with both CPU and GPU. MLP generally takes the least time because of its simple architecture, followed by GCN, GAT, EGCN, and CNN; however, when GPU is used, EGCN shows a faster computational time than GAT. When comparing CPU and GPU performances for deep learning models, GPU always outperforms CPU, speeding

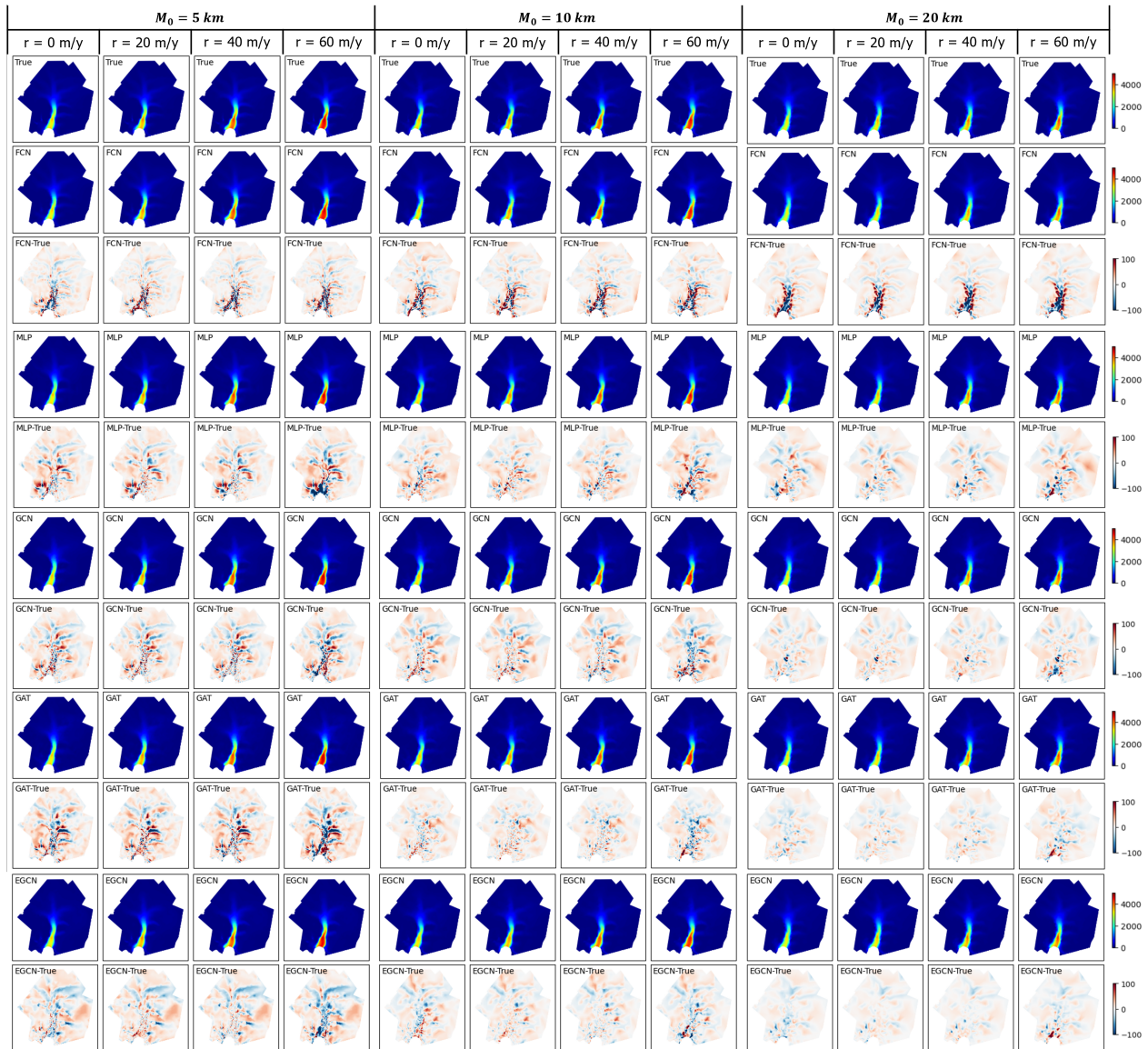


**Figure 5.** Maps of ice velocity modeled by the ISSM simulation (indicated as True) and difference with deep-learning emulators (FCN, MLP, GCN, GAT, and EGCN) for different basal melting rates ( $r$ ) and initial mesh sizes ( $M_0$ ). All maps are bilinearly interpolated from the node predictions and represent the average of 20-year results.

up by 3-40 times. The most dramatic speed-up by replacing GPU with CPU occurs with EGCN: the computational time of the EGCN speeds up by 38, 44, and 25 times using CPU for 5 km, 10 km, and 20 km of initial mesh size, respectively. When GPU is used, the computation time of MLP is 100-200 times faster than that of ISSM, and GNNs show 15-50 times faster computation time than the ISSM. The FCN shows the least speed-up among other deep learning emulators: 6-15 times faster computational time than ISSM when using GPU. The longest elapsed time of FCN is attributed to its requirement for regular grid format. Since FCN is implemented on regular grids for all locations with fixed resolution, it cannot efficiently allocate computational resources in accordance with computational complexity. However, since GNNs are implemented on adjusted meshes, computational resources can be efficiently allocated to where a more detailed resolution and computational complexity are necessary. In this aspect, we emphasize that the speed-up by GPU-based emulators is more significant for a fine mesh size ( $M_0 = 5$  km) than a coarse mesh size ( $M_0 = 20$  km). This implies that the GNN emulators can be more efficient for complex and high-resolution ice sheet modeling than traditional FCN emulators.

**Table 3.** Total computational time (in seconds) for producing final ice sheet transient simulations for 20 years and 36 different melting rates. The fastest emulator is highlighted in bold.

	Model	$M_0 = 5$ km		$M_0 = 10$ km		$M_0 = 20$ km	
		CPU	GPU	CPU	GPU	CPU	GPU
Simulation	ISSM	712.96	-	399.78	-	209.85	-
Emulator	FCN	1932.00	33.34	1859.65	33.27	1834.68	32.93
	MLP	<b>25.02</b>	<b>2.99</b>	<b>11.72</b>	<b>2.37</b>	<b>6.76</b>	<b>1.91</b>
	GCN	125.05	14.18	60.37	11.83	34.50	11.99
	GAT	467.78	16.50	216.72	13.73	104.16	13.13
	EGCN	607.77	16.14	282.46	6.36	134.31	5.29

## Discussion

Since the deep-learning emulators reduce computational time dramatically, they can be useful for a fast sensitivity analysis to investigate the impacts of environmental parameters on the behavior of ice sheets. Considering that accelerated ocean warming in the Amundsen Sea is the main driver for ice sheet melting in the west Antarctic during the 21st century<sup>19-21</sup>, we use our emulators to examine how the total ice volume and mean ice velocity change with different basal melting rate scenarios. The total ice volumes and mean ice velocities by different melting rates ranging from 0 to 70 are retrieved by the ISSM simulations and deep-learning emulators (Fig. 6). Regarding the total ice volume (Fig. 6a), most deep learning models reproduce the decrease in ice volume with higher melting rates. If the melting rate changes from 0 to 70 m/year, the ISSM and most deep-learning emulators predict that the PIG will lose 2,300-3,100 km<sup>3</sup> of more ice after 20 years. While the ice volumes retrieved from emulators with 5 km and 20 km  $M_0$  seem relatively stable, significant overestimation and underestimation are found in the 10 km  $M_0$  experiment, especially at higher melting rates. This shows the importance of selecting a proper mesh resolution when using GNN emulators. MLP shows an abrupt rise in ice volume at a melting rate greater than 60 m/year on 5 km and 10 km  $M_0$ , which is not scientifically plausible. GAT and EGCN also overestimate ice volume at higher melting rates on 10 km  $M_0$ . On the other hand, it is noted that GCN underestimates the ice volume significantly at melting rates greater than 40 m/year on 10 km  $M_0$ . Although FCN shows a similar decreasing trend of ice volume with higher melting rates, the FCN result is negatively biased to the ISSM result by around 1,500-1,800 km<sup>3</sup>.

The mean ice velocity generally increases for higher melting rates (Fig. 6b), which are reproduced by the ISSM and all machine learning emulators successfully. If the melting rate changes from 0 to 70 m/year, the mean ice velocity increases by up to 50-100 km/year after 20 years. Similar to the ice thickness experiment, MLP shows abnormal variations in ice velocity at melting rates greater than 60 m/year. MLP underestimates ice velocity on 5 km  $M_0$  at melting rates greater than 60 m/year, whereas it overestimates on 10 km and 20 km  $M_0$ . Such a higher uncertainty by MLP may be attributed to its architecture that cannot intrinsically utilize neighboring node information. All other GNN emulators show similar prediction results with each other and ISSM. Herein, it should be noted that the overall variation in ice velocity is substantially sensitive to mesh size compared to the ice volume experiment. In the 5 km  $M_0$  experiment of year 20, ice velocity increases by 100 m/year from 0 to 70 m/year melting rate. However, in the 10 km and 20 km  $M_0$  experiments, the increase in ice velocity reaches only 90 and 50 m/year, respectively. Since too-coarse mesh resolution cannot describe detailed velocity distributions, it is advisable to use fine mesh resolution enough to capture detailed ice flow. As discussed in Table 3, our emulators would be more beneficial for such a fine mesh resolution ice sheet modeling, reducing more computational time without losing significant accuracy.

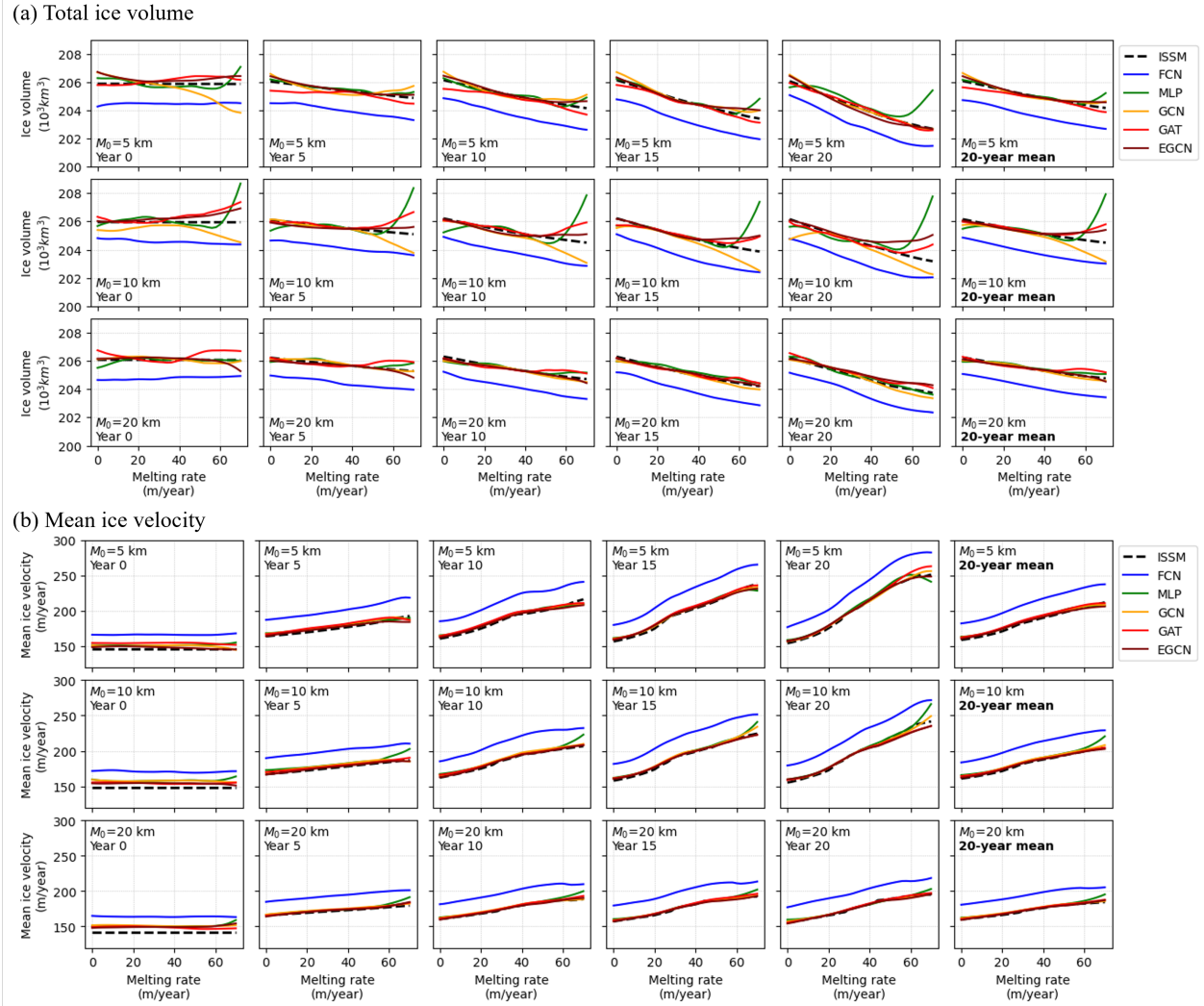


**Figure 6.** (a) Total ice volume and (b) mean ice velocity by melting rates from 0 to 70 for every five years and different mesh resolutions. The rightmost panel is the average of 20 years.

## Methods

In this study, we train and test three GNNs (GCN, GAT, and EGCN), along with two traditional baseline machine learning models (MLP and CNN). This section explains the detailed architectures of these neural networks and how they are trained.

### Graph Convolutional Network (GCN)

The GCN of this study consists of graph convolutional layers, which are inspired by the localized first-order approximation of spectral graph convolutions on graph-structured data<sup>22</sup>. Let the  $l$ th graph convolutional layer receives a set of node features  $\mathbf{h}^{(l)} = \{h_1^{(l)}, h_2^{(l)}, \dots, h_N^{(l)}\}$ ,  $h_i^{(l)} \in \mathbb{R}^{F_l}$  as the input and produces a new set of node features,  $\mathbf{h}^{(l+1)} = \{h_1^{(l+1)}, h_2^{(l+1)}, \dots, h_N^{(l+1)}\}$ ,  $h_i^{(l+1)} \in \mathbb{R}^{F_{l+1}}$ , for the next  $l + 1$ th layer.  $N$  is the number of nodes;  $F_l$  and  $F_{l+1}$  is the number of features in each node at  $l$ th layer and  $l + 1$  layer, respectively. Then, the layer-wise propagation rule of the graph convolutional layer is defined by following equation:

$$h_i^{(l+1)} = \sigma \left( \sum_{j \in \mathcal{N}(i)} \frac{e_{ij}}{c_{ij}} \mathbf{W}^{(l)} h_j^{(l)} \right) \quad (1)$$

$$e_{ij} = \exp \left( - \frac{1}{\sqrt{(x_i - x_j)^2 + (y_i - y_j)^2}} \right)$$



where  $\mathcal{N}(i)$  is the set of neighbors of node  $i$ ,  $c_{ij}$  is the product of the square root of node degrees (i.e.,  $c_{ij} = \sqrt{|\mathcal{N}(j)|} \sqrt{|\mathcal{N}(i)|}$ ),  $e_{ij}$  is the scalar weight determined by the spatial distance between node  $i$  and node  $j$ . The  $x, y$  coordinates and node  $i$  and node  $j$  are denoted by  $(x_i, y_i)$  and  $(x_j, y_j)$ , respectively.  $\mathbf{W}^{(l)}$  is a layer-specific trainable weight matrix ( $\mathbf{W}^{(l)} \in \mathbb{R}^{F_{l+1} \times F_l}$ ), and  $\sigma(\cdot)$  is an activation function; we use the Leaky ReLU activation function of 0.01 negative slope in this study.

### Graph Attention Network (GAT)

A graph attention layer can be defined by the following equation with respect to  $h_i^{(l)}$  and  $h_i^{(l+1)}$ <sup>23</sup>:

$$h_i^{(l+1)} = \sigma\left(\sum_{j \in \mathcal{N}(i)} \alpha_{ij}^{(l)} \mathbf{W}^{(l)} h_j^{(l)}\right) \quad (2)$$

where  $\alpha^{(l)}$  is the attention score between node  $i$  and node  $j$  defined as follows:

$$\alpha_{ij}^{(l)} = \text{softmax}_j(e_{ij}^{(l)}) = \frac{\exp(e_{ij}^{(l)})}{\sum_{k \in \mathcal{N}(i)} \exp(e_{ik}^{(l)})} \quad (3)$$

$$e_{ij}^{(l)} = a(\mathbf{W}^{(l)} h_i^{(l)}, \mathbf{W}^{(l)} h_j^{(l)})$$

Herein,  $a: \mathbb{R}^{F_{l+1}} \times \mathbb{R}^{F_{l+1}} \rightarrow \mathbb{R}$  is a self-attention mechanism to compute attention coefficient  $e_{ij}^{(l)}$ . In our experiments, this attention mechanism  $a$  is a single-layer feedforward neural network parameterized by a weight vector  $\bar{\mathbf{a}} \in \mathbb{R}^{2F_{l+1}}$ , normalized by LeakyReLU function afterward. The graph structure is applied to this attention mechanism by computing  $e_{ij}^{(l)}$  for only nodes  $j \in \mathcal{N}(i)$  where  $\mathcal{N}(i)$  is set of neighbors of node  $i$ . Thus, the attention score  $\alpha^{(l)}$  can be expressed as follows:

$$\alpha_{ij}^{(l)} = \frac{\exp(\text{LeakyReLU}(\bar{\mathbf{a}}^T [\mathbf{W}^{(l)} h_i^{(l)} \parallel \mathbf{W}^{(l)} h_j^{(l)}]))}{\sum_{k \in \mathcal{N}(i)} \exp(\text{LeakyReLU}(\bar{\mathbf{a}}^T [\mathbf{W}^{(l)} h_i^{(l)} \parallel \mathbf{W}^{(l)} h_k^{(l)}]))} \quad (4)$$

where  $^T$  denotes transpose operation and  $\parallel$  is the concatenation operation. Moreover, we execute  $K$  independent attention mechanisms of Equation 2 and average them for the final graph attention layer<sup>23</sup>. In this study, we employ 3 multi-head at the final graph attention layer.

### Equivariant Graph Convolutional Network (EGCN)

Another graph neural network we employ is the EGCN, which is designed to conserve equivariance to rotations, translations, reflections, and permutations in a graph structure<sup>24</sup>. We expect that this EGCN structure should guarantee more general applicability to any mesh or graph structure than other GNNs because it preserves equivariance to rotations and translations on a set of spatial coordinates and also preserves equivariance to permutations on the set of nodes. As a modified version of the graph convolutional network<sup>25</sup>, which adopted a message-passing algorithm and aggregation procedure, an equivariant graph convolutional layer can be expressed by the following series of equations:

$$m_{ij} = \phi_e(h_i^{(l)}, h_j^{(l)}, \|x_i^{(l)} - x_j^{(l)}\|^2, a_{ij}) \quad (5)$$

$$x_i^{(l+1)} = x_i^{(l)} + C \sum_{j \neq i} (x_i^{(l)} - x_j^{(l)}) \phi_x(m_{ij}) \quad (6)$$

$$m_i = x_i^{(l)} + C \sum_{j \neq i} m_{ij} \quad (7)$$

$$h_i^{(l+1)} = \phi_h(h_i^{(l)}, m_i) \quad (8)$$

where  $a_{ij}$  is the edge attributes,  $x_i$  and  $x_j$  are the coordinate embeddings for node  $i$  and  $j$ , respectively, and  $C$  is a constant for normalization computed as  $1/|\mathcal{N}(i)|$ .  $\phi_e$ ,  $\phi_x$ , and  $\phi_h$  are the edge, position, and node operations, respectively, which are approximated by MLPs. The translation and rotation equivariance can be preserved through Equation 6<sup>24</sup>. Additionally, this equivariant operation is very flexible since the embedding message  $m_{ij}$  can carry information from the entire graph and not only from the specific neighboring nodes<sup>24</sup>.

## Multi-layer perception (MLP)

As a baseline model as a deep learning emulator, we train and test an MLP model. In the MLP model, all the five graph convolutional layers of GNNs are replaced into fully connected layers (Fig 1). Consequently, the MLP consists of one input layer (4 features), five hidden layers (128 features), and one output layer (3 features). The leaky ReLU activation function of 0.01 negative slope is applied after each hidden layer. Although this MLP model implements a node regression task, it does not necessarily embed edge information or connections between nodes in the graph structure.

## Convolutional Neural Network (CNN)

We also train and test a fully convolutional network (FCN), a type of convolutional neural network (CNN), as a baseline machine learning model to compare with GNNs. The FCN consists of five hidden convolutional layers; all the graph convolutional layers and fully connected layers of GNNs are replaced with 2-D convolutional layers with a kernel size of 3 and filter size of 128 (Fig. 1). The leaky ReLU activation function of 0.01 negative slope is applied after each convolutional layer. Since the FCN takes regular grids as the input and output, we interpolate all the irregular mesh construction of the ISSM simulation into a 1 km grid. These 1 km grid datasets are used as the input and output of the FCN, but the output of the FCN is sampled again to be compared with the mesh-structured GCN output.

## ISSM model simulation for the Pine Island Glacier

To generate training datasets for the deep learning emulators, we run 20-year transient simulations of ice thickness and ice velocity in the PIG by following the previous studies of ISSM-based sensitivity experiments<sup>26,27</sup>. Since the PIG has a significant portion of floating ice, we use the Shallow Shelf Approximation (SSA)<sup>8</sup> to explain ice flow as follows:

$$\frac{\partial}{\partial x} \left( 4H\mu \frac{\partial u}{\partial x} + 2H\mu \frac{\partial v}{\partial y} \right) + \frac{\partial}{\partial y} \left( H\mu \frac{\partial u}{\partial y} + H\mu \frac{\partial v}{\partial x} \right) = \rho g H \frac{\partial s}{\partial x} \quad (9)$$

$$\frac{\partial}{\partial y} \left( 4H\mu \frac{\partial v}{\partial y} + 2H\mu \frac{\partial u}{\partial x} \right) + \frac{\partial}{\partial x} \left( H\mu \frac{\partial u}{\partial y} + H\mu \frac{\partial v}{\partial x} \right) = \rho g H \frac{\partial s}{\partial y} \quad (10)$$

where  $(u, v, w)$  are the  $x, y,$  and  $z$  components of the ice velocity vector  $\mathbf{v}$  in the Cartesian coordinate system ( $z$  is the vertical direction),  $H$  is the local ice thickness,  $\mu$  is the effective ice viscosity,  $\rho$  is ice density, and  $g$  is acceleration due to gravity. As for the datasets, we collect ice velocity data from the NASA Making Earth System Data Records for Use in Research Environments (MEaSUREs)<sup>28</sup> (Fig.7b), 1 km Antarctic digital elevation model (DEM) data<sup>29</sup> (Fig.7c), bedrock topography data of the Amundsen Sea continental shelf<sup>30</sup> (Fig.7d), Antarctic surface temperature data<sup>31</sup>, Antarctic surface mass balance data<sup>32</sup>, and Antarctic geothermal heat flux data<sup>33</sup>.

We run the simulations on three different mesh sizes: 5 km, 10 km, and 20 km initial mesh sizes ( $M_0$ ). For different mesh size experiments, mesh size is adjusted by ice velocity after the initialization. The 5 km, 10 km, and 20 km mesh initialization generates the final mesh grid with 4739, 2085, and 931 elements, respectively, corresponding to 2468, 1112, and 526 nodes. We conduct the ISSM simulations for different annual basal melting rates ranging from 0 to 70 m/year for every 2 m/year. Transient simulations are run forward for 20 years with time steps of one month. Consequently, we execute 20-year (240-month) transient simulations 108 times: 3 different mesh sizes and 36 different melting rates. All ISSM simulations are implemented on a MATLAB environment with an Intel(R) Core(TM) i7-11700F CPU with 8 2.5 GHz cores.

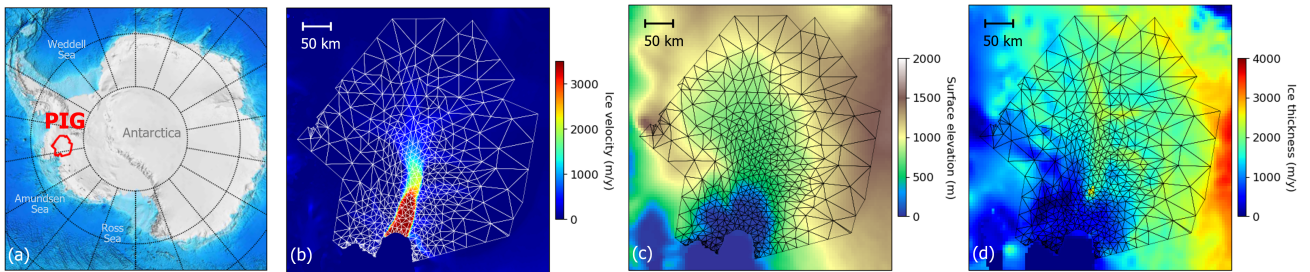


**Figure 7.** (a) Location of the Pine Island Glacier (PIG) in Antarctica. (b) Ice velocity data, (c) surface height data, and (d) ice thickness data overlapped with the generated mesh ( $M_0=20$  km).

## Training and testing graph neural networks

A total of 25,920 graph structures (240 months  $\times$  3 mesh sizes  $\times$  36 basal melting rates) are collected from the ISSM transient simulations. All nodes of these graphs contain four input features (i.e., x and y coordinates on the Antarctic Polar Stereographic projection, time, and basal melting rate) and three output features (i.e., x-component and y-component ice velocity and ice thickness), which are used to train deep-learning emulators. The input feature values are normalized into [-1, 1] based on the nominal maximum and minimum values that each variable can have. In graph structures, the connectivity of nodes is determined from the finite mesh element: if two nodes are connected in a mesh element, these nodes are also connected by edges (Fig 1). All 25,920 graph structures are divided into train, validation, and test datasets based on the melting rate values: melting rates of 10, 30, 50, and 70 m/year are used for validation, melting rates of 0, 20, 40, and 60 m/year are used for testing, and the remainders are for training. As a result, the number of train, validation, and test datasets is 20,160, 2,880, and 2,880, respectively. We use the mean square error (MSE) as the loss function, and the model is optimized by Adam stochastic gradient descent algorithm with 200 epochs and 0.01 learning rate. All deep learning models are trained on the Python environment using the Deep Graph Library (DGL) and PyTorch modules. In measuring the computational time (Table 3), we record the time to generate the final results of 20-year ice thickness and velocity for all 36 melting rates. Two computational resources of the same desktop (Lenovo Legion T5 26IOB6) are compared: a CPU (Intel(R) Core(TM) i7-11700F) and a GPU (NVIDIA RTX A5000).

## References

1. Otosaka, I. N. *et al.* Mass balance of the greenland and antarctic ice sheets from 1992 to 2020. *Earth Syst. Sci. Data* **15**, 1597–1616, DOI: [10.5194/essd-15-1597-2023](https://doi.org/10.5194/essd-15-1597-2023) (2023).
2. Joughin, I., Shapero, D., Smith, B., Dutriex, P. & Barham, M. Ice-shelf retreat drives recent pine island glacier speedup. *Sci. Adv.* **7**, eabg3080, DOI: [10.1126/sciadv.abg3080](https://doi.org/10.1126/sciadv.abg3080) (2021). <https://www.science.org/doi/pdf/10.1126/sciadv.abg3080>.
3. Joughin, I., Shapero, D., Dutriex, P. & Smith, B. Ocean-induced melt volume directly paces ice loss from pine island glacier. *Sci. Adv.* **7**, eabi5738, DOI: [10.1126/sciadv.abi5738](https://doi.org/10.1126/sciadv.abi5738) (2021). <https://www.science.org/doi/pdf/10.1126/sciadv.abi5738>.
4. Jacobs, S. S., Jenkins, A., Giulivi, C. F. & Dutriex, P. Stronger ocean circulation and increased melting under pine island glacier ice shelf. *Nat. Geosci.* **4**, 519–523 (2011).
5. Rignot, E. *et al.* Four decades of antarctic ice sheet mass balance from 1979–2017. *Proc. Natl. Acad. Sci.* **116**, 1095–1103, DOI: [10.1073/pnas.1812883116](https://doi.org/10.1073/pnas.1812883116) (2019). <https://www.pnas.org/doi/pdf/10.1073/pnas.1812883116>.
6. Glen, J. W. & Perutz, M. F. The creep of polycrystalline ice. *Proc. Royal Soc. London. Ser. A. Math. Phys. Sci.* **228**, 519–538, DOI: [10.1098/rspa.1955.0066](https://doi.org/10.1098/rspa.1955.0066) (1955). <https://royalsocietypublishing.org/doi/pdf/10.1098/rspa.1955.0066>.
7. Hutter, K. *Theoretical Glaciology: Material Science of Ice and the Mechanics of Glaciers and Ice Sheets*. Mathematical Approaches to Geophysics (Springer, 1983).
8. MacAyeal, D. R. Large-scale ice flow over a viscous basal sediment: Theory and application to ice stream b, antarctica. *J. Geophys. Res. Solid Earth* **94**, 4071–4087, DOI: <https://doi.org/10.1029/JB094iB04p04071> (1989). <https://agupubs.onlinelibrary.wiley.com/doi/pdf/10.1029/JB094iB04p04071>.
9. Blatter, H. Velocity and stress fields in grounded glaciers: a simple algorithm for including deviatoric stress gradients. *J. Glaciol.* **41**, 333–344, DOI: [10.3189/S002214300001621X](https://doi.org/10.3189/S002214300001621X) (1995).
10. Pattyn, F. Numerical modelling of a fast-flowing outlet glacier: experiments with different basal conditions. *Annals Glaciol.* **23**, 237–246, DOI: [10.3189/S0260305500013495](https://doi.org/10.3189/S0260305500013495) (1996).
11. Morlighem, M. *et al.* Spatial patterns of basal drag inferred using control methods from a full-stokes and simpler models for pine island glacier, west antarctica. *Geophys. Res. Lett.* **37**, DOI: <https://doi.org/10.1029/2010GL043853> (2010). <https://agupubs.onlinelibrary.wiley.com/doi/pdf/10.1029/2010GL043853>.
12. Larour, E., Seroussi, H., Morlighem, M. & Rignot, E. Continental scale, high order, high spatial resolution, ice sheet modeling using the ice sheet system model (issm). *J. Geophys. Res. Earth Surf.* **117**, DOI: <https://doi.org/10.1029/2011JF002140> (2012). <https://agupubs.onlinelibrary.wiley.com/doi/pdf/10.1029/2011JF002140>.
13. Jouvet, G. *et al.* Deep learning speeds up ice flow modelling by several orders of magnitude. *J. Glaciol.* **68**, 651–664, DOI: [10.1017/jog.2021.120](https://doi.org/10.1017/jog.2021.120) (2022).
14. Jouvet, G. & Cordonnier, G. Ice-flow model emulator based on physics-informed deep learning. *J. Glaciol.* 1–15, DOI: [10.1017/jog.2023.73](https://doi.org/10.1017/jog.2023.73) (2023).
15. Jouvet, G. Inversion of a stokes glacier flow model emulated by deep learning. *J. Glaciol.* **69**, 13–26, DOI: [10.1017/jog.2022.41](https://doi.org/10.1017/jog.2022.41) (2023).

16. He, Q., Perego, M., Howard, A. A., Karniadakis, G. E. & Stinis, P. A hybrid deep neural operator/finite element method for ice-sheet modeling. *J. Comput. Phys.* **492**, 112428, DOI: <https://doi.org/10.1016/j.jcp.2023.112428> (2023).
17. Lu, L., Jin, P., Pang, G., Zhang, Z. & Karniadakis, G. E. Learning nonlinear operators via deepnet based on the universal approximation theorem of operators. *Nat. machine intelligence* **3**, 218–229 (2021).
18. Zhang, S., Tong, H., Xu, J. & Maciejewski, R. Graph convolutional networks: a comprehensive review. *Comput. Soc. Networks* **6**, 1–23 (2019).
19. Naughten, K. A., Holland, P. R. & De Rydt, J. Unavoidable future increase in west antarctic ice-shelf melting over the twenty-first century. *Nat. Clim. Chang.* **13**, 1222–1228, DOI: [10.1038/s41558-023-01818-x](https://doi.org/10.1038/s41558-023-01818-x) (2023).
20. Naughten, K. A. *et al.* Future projections of antarctic ice shelf melting based on cmip5 scenarios. *J. Clim.* **31**, 5243 – 5261, DOI: [10.1175/JCLI-D-17-0854.1](https://doi.org/10.1175/JCLI-D-17-0854.1) (2018).
21. Jourdain, N. C., Mathiot, P., Burgard, C., Caillet, J. & Kittel, C. Ice shelf basal melt rates in the amundsen sea at the end of the 21st century. *Geophys. Res. Lett.* **49**, e2022GL100629, DOI: <https://doi.org/10.1029/2022GL100629> (2022). E2022GL100629 2022GL100629, <https://agupubs.onlinelibrary.wiley.com/doi/pdf/10.1029/2022GL100629>.
22. Kipf, T. N. & Welling, M. Semi-supervised classification with graph convolutional networks, DOI: [10.48550/arXiv.1609.02907](https://doi.org/10.48550/arXiv.1609.02907) (2017). [1609.02907](https://arxiv.org/abs/1609.02907).
23. Veličković, P. *et al.* Graph attention networks, DOI: [10.48550/arXiv.1710.10903](https://doi.org/10.48550/arXiv.1710.10903) (2018). [1710.10903](https://arxiv.org/abs/1710.10903).
24. Satorras, V. G., Hoogeboom, E. & Welling, M. E(n) equivariant graph neural networks, DOI: [10.48550/arXiv.2102.09844](https://doi.org/10.48550/arXiv.2102.09844) (2022). [2102.09844](https://arxiv.org/abs/2102.09844).
25. Gilmer, J., Schoenholz, S. S., Riley, P. F., Vinyals, O. & Dahl, G. E. Neural message passing for quantum chemistry (2017). [1704.01212](https://arxiv.org/abs/1704.01212).
26. Seroussi, H. *et al.* Sensitivity of the dynamics of pine island glacier, west antarctica, to climate forcing for the next 50 years. *The Cryosphere* **8**, 1699–1710, DOI: [10.5194/tc-8-1699-2014](https://doi.org/10.5194/tc-8-1699-2014) (2014).
27. Larour, E. *et al.* Sensitivity analysis of pine island glacier ice flow using issm and dakota. *J. Geophys. Res. Earth Surf.* **117**, DOI: <https://doi.org/10.1029/2011JF002146> (2012). <https://agupubs.onlinelibrary.wiley.com/doi/pdf/10.1029/2011JF002146>.
28. Mouginot, J., Scheuchl, B. & Rignot, E. Measures annual antarctic ice velocity maps, version 1, DOI: [10.5067/9T4EPQXTJYW9](https://doi.org/10.5067/9T4EPQXTJYW9) (2017).
29. Bamber, J. L., Gomez-Dans, J. L. & Griggs, J. A. A new 1 km digital elevation model of the antarctic derived from combined satellite radar and laser data – part 1: Data and methods. *The Cryosphere* **3**, 101–111, DOI: [10.5194/tc-3-101-2009](https://doi.org/10.5194/tc-3-101-2009) (2009).
30. Nitsche, F. O., Jacobs, S. S., Larter, R. D. & Gohl, K. Bathymetry of the amundsen sea continental shelf: Implications for geology, oceanography, and glaciology. *Geochem. Geophys. Geosystems* **8**, DOI: <https://doi.org/10.1029/2007GC001694> (2007). <https://agupubs.onlinelibrary.wiley.com/doi/pdf/10.1029/2007GC001694>.
31. Comiso, J. C. Variability and trends in antarctic surface temperatures from in situ and satellite infrared measurements. *J. Clim.* **13**, 1674 – 1696, DOI: [10.1175/1520-0442\(2000\)013<1674:VATIAS>2.0.CO;2](https://doi.org/10.1175/1520-0442(2000)013<1674:VATIAS>2.0.CO;2) (2000).
32. Vaughan, D. G., Bamber, J. L., Giovinetto, M., Russell, J. & Cooper, A. P. R. Reassessment of net surface mass balance in antarctica. *J. Clim.* **12**, 933 – 946, DOI: [10.1175/1520-0442\(1999\)012<0933:RONSMB>2.0.CO;2](https://doi.org/10.1175/1520-0442(1999)012<0933:RONSMB>2.0.CO;2) (1999).
33. Maule, C. F., Purucker, M. E., Olsen, N. & Mosegaard, K. Heat flux anomalies in antarctica revealed by satellite magnetic data. *Science* **309**, 464–467, DOI: [10.1126/science.1106888](https://doi.org/10.1126/science.1106888) (2005). <https://www.science.org/doi/pdf/10.1126/science.1106888>.

### Acknowledgements

This work is supported by NSF BIGDATA (IIS-1838230, 2308649) and NSF Leadership Class Computing (OAC-2139536) awards.